CHARACTERIZATION OF OXIDES FORMED ON MODEL ZIRCONIUM ALLOYS IN 360°C WATER USING MICRO-BEAM SYNCHROTRON RADIATION

A. Yilmazbayhan[1], Marcelo Gomes da Silva[1], Arthur Motta[1], Hyun-Gil Kim[2], Yong Hwan Jeong[2], Jeong-Yong Park[2], Robert Comstock[3], Barry Lai[4], Zhounghou Cai[4]

[1]Dept. of Mechanical and Nuclear Engineering, The Pennsylvania State University, University Park, PA 16802, USA.
[2]Zr Fuel Cladding Team, Korea Atomic Energy Research Institute, Daejeon 305-353, Republic of Korea
[3]Science and Technology Dept., Westinghouse Electric Co., Pittsburgh, PA 15235-5082, USA
[4]Advanced Photon Source, Argonne National Laboratory, Argonne, IL, 60439, USA
Keywords: Zirconium alloys, oxides, synchrotron radiation

Abstract

Uniform oxidation by the primary circuit water may limit the service of Zr alloy fuel cladding in Light Water Reactors, especially under more severe fuel duty cycles. Understanding the impact of alloy chemistry and microstructure on corrosion performance may allow us to design better alloys for severe duty cycle applications. To undertake such research, model zirconium alloys (Zr-xCr-yFe, Zr-xCu-yMo, Zr-xSn and Zr-xNb, with various values of x and y) were corroded at 360 $^{\circ}$C in pure water to help isolate the role of individual alloying elements on the oxide formation process. The structure of the protective oxide, believed to be the cause for the different corrosion behavior of different zirconium alloys, was investigated using microbeam synchrotron radiation diffraction. Experiments were conducted at both the Advanced Photon Source in the USA using a 0.25 micron beam, and in the Pohang Light Source, Korea, using a 1.25 micron beam. Such micro-diffraction experiments allow the determination of phases present, oxide texture, grain size and accumulated stress, as a function of distance from the oxide-metal interface. Additional examinations were performed using cross-sectional transmission electron microscopy (TEM). The results of this examination show heretofore unobserved details of the oxide-metal interface and of the variation of phase content with distance from oxide-metal interface and overall oxide thickness. We focus in this paper on the evolution of oxide texture and phase content, between the different model alloys to help elucidate the role of individual alloying elements on the oxide formation process.

Introduction

Waterside corrosion of nuclear fuel cladding and associated hydriding is one of the factors that limit fuel duty in nuclear reactors. If corrosion rates can be reduced by proper choice of alloys, then considerable savings can be realized. Modern alloys have shown considerable improvement in corrosion behavior over older alloys such as Zircaloy-4 and even low-Sn Zircaloy-4 [1]. In fact it is a common observation that changing the composition of Zr alloys by comparatively small amounts yields significant differences in corrosion behavior for these alloys. This was known even from the time of the development of Zircaloys, as they represent relatively small departures (~ 2%) from pure Zr which is known to exhibit poor corrosion behavior [2].

Although the compositions, heat treatments and microstructure that optimize corrosion resistance of Zr alloys are well known empirically, the underlying mechanistic reason for these differences is still not known. That is, the question of how the alloying elements improve corrosion behavior is largely unanswered. In a recent paper it was proposed that the difference in corrosion behavior originates in the different structures of the protective oxide formed in these alloys [3]. The hypothesis is based on autoclave tests that showed differences in the corrosion behavior, highlighting the importance of the alloy in determining corrosion rate.

In previous studies the microstructure of the oxides formed on commercial alloys was studied using microbeam synchrotron radiation and transmission electron microscopy [3, 4]. The mechanistic connections between the oxide microstructure and the alloy microstructure are more complex to discern in these alloys as commercial alloys have many different alloying elements. As a result, it is not easy to separate the effects of individual alloying elements on the corrosion process.

This paper reports on a current research project designed to elucidate some of these questions. Long-term autoclave corrosion tests were performed on model alloys to understand individual role of alloying elements on corrosion. The set of alloys includes both alloying elements that form either solid solutions or that form precipitates. The corrosion results are presented along with the results of the microstructure examination of these alloy oxides, focusing on the determination of oxide tetragonal fraction and oxide crystallographic texture.

Experimental Methods

Twenty-six model Zr alloys were prepared for this study. The alloys can be classified into three groups: a. fifteen alloys contain precipitates, b. eight alloys have solute additions, and c. three serve as reference materials. These alloys were selected to identify the role of precipitates or solute atoms on corrosion. The target chemical compositions of the three groups of model alloys are shown in Table 1.

The alloys were prepared by arc melting in vacuum followed by heat treatment in the beta phase, hot rolling, and a

succession of cold rolling and annealing steps to produce sheets of the desired material. The annealing temperatures were 580 ^{o}C, 650 ^{o}C and 720 ^{o}C, to achieve particular microstructures. These heat treatments produced samples in the recrystallized condition and with relatively small grain size. The alloys were characterized using synchrotron radiation x-ray powder diffraction in a manner similar to what was described in [5] and the target precipitate structures and sizes were observed. The types of precipitates identified and their approximate size and volume fraction are also shown in Table 1. It is apparent from Table 1 that synchrotron radiation allows a level of characterization of the metallic alloy microstructure that can help highlight the specific role of individual alloy features on the corrosion process.

From these sheets approximately 60 corrosion coupons of each alloy were fabricated. After grinding the coupon surfaces and engraving an identification number, the coupons were pickled to provide a reproducible surface for corrosion. The model alloys were corrosion tested in 360°C pure water at saturation pressure. The test was periodically stopped, the samples taken out of the autoclave, and the weight gain measured. Two autoclaves tests were run for each alloy: in the first one, frequent weight gain measurements were performed (1, 3, 7, 14, 28, 42, and 56 days) to characterize the pre-transition corrosion kinetics of the alloys, and in the second one, the weight gain measurements were less frequent, with the goal of characterizing the longer term or post-transition corrosion kinetics. The oxide samples were examined using x-ray synchrotron radiation at the Advanced Photon Source (APS) at Argonne and at Pohang Light Source in Republic of Korea to determine the detailed oxide microstructure and relate this to corrosion rate. The use of synchrotron radiation in general is beneficial for several reasons: the very high number of photons available makes the experiments practical as they can be conducted quickly; the low background and instrumental broadening allows for very well defined peaks and for the ability to detect small amounts of second phase [6]. In the microbeam line (2ID-D at APS) specifically, the concentration of such high photon flux into a sub-micron region permits the study of the oxide with an unparalleled combination of spatial resolution and structure definition.

Various experimental geometries were used, as illustrated in Figure 1. The geometry used in Figure 1(a) consists of a cross sectional oxide sample, which is examined using a microbeam (0.25 x 0.3 micron) which is scanned across the oxide so that spatially resolved information can be obtained. Using a CCD area detector the diffraction peaks from the oxide are obtained and integrated to yield a plot of diffracted intensity vs. two theta angle. This allows us to identify and study the phases present, texture and grain size as a function of distance from the oxide metal interface. In the second geometry (Figure 1(b)), transmission geometry was used to allow for more complete determination of oxide texture and its variation within the oxide. For this experiment, a cross sectional oxide sample is prepared with an overall oxide thickness of 10-20 micron by polishing and dimpling. The 9.5 keV microbeam is incident on the sample and transverses it creating the diffraction cones captured on the
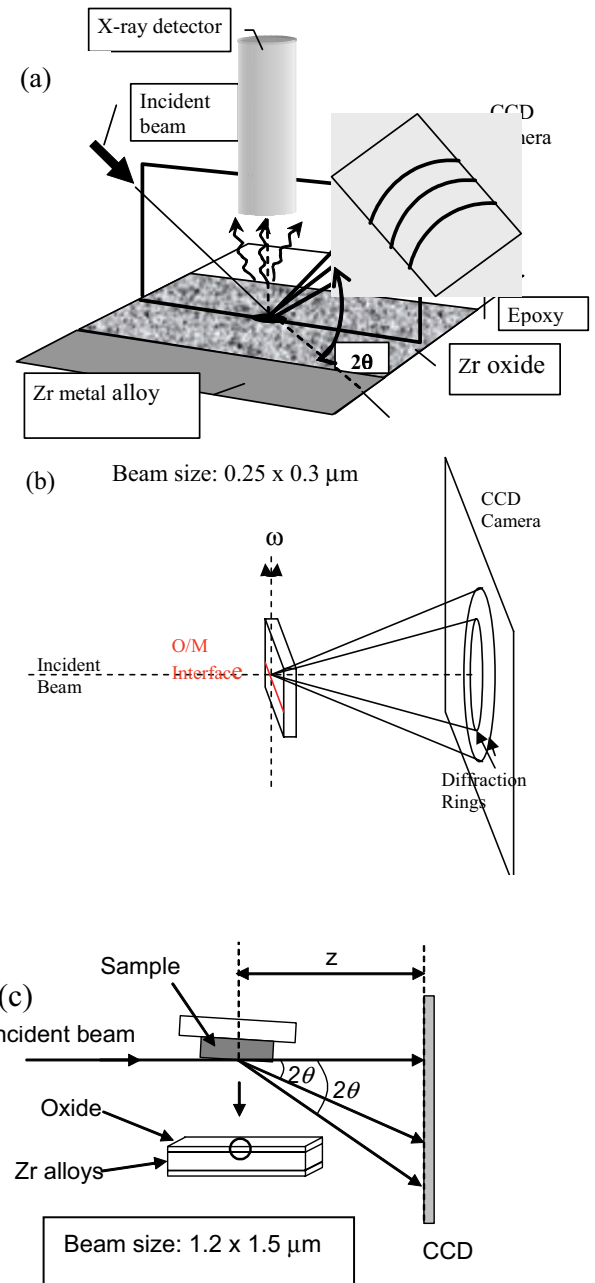

Figure 1: Experimental geometries used (a) Reflection mode and (b) Transmission mode experimental setup (both at 2IDD at APS), and (c) at the micron-size beam line in Korea.

CCD camera. By piecewise integrating the diffraction ellipses (equivalent to varying the azimuthal angle phi) and by varying the angle ω, a wide range of sample orientations can be investigated, which allows the generation of pole figures. This allows for the first time to study the crystallographic texture of the oxide phases and the texture gradient in the oxide at the sub-micron level. This means that the orientation relationships, texture gradients and general phase evolution in the growing oxide can be studied. In the third geometry (Fig. 1(c)) variable angle grazing incidence is used to obtain depth information.

Table 1: Characteristics of the alloys examined in this study

| Alloy system	Composition (wt.%)	Precipitate Characteristics		
		Crystal Structure	Size (nm)	Volume Fraction
Zr-Nb	Zr-0.2, 0.4, 1.0, 1.5, 2.5Nb	hcp $Zr(Nb,Fe)_2$, bcc β-Nb and orthor. Zr_3Fe	75-110	Increases as Nb content increases (0-2.3%)
Zr-Fe-Cr	Zr-0.4Fe-0.2Cr and Zr-0.2Fe-0.1Cr (two processing temperatures: 580 °C (L) and 720 °C (H))	Cubic and hex. $Zr(Cr,Fe)_2$	35-107	~1%
Zr-Cr-Fe	Zr0.5Cr, Zr-0.5Cr-0.2Fe, Zr-1.0Cr, Zr-1.0Cr-0.2Fe	Cubic $ZrCr_2$ and cubic $Zr(Cr,Fe)_2$	40-60	~1-1.5%
Zr-Cu-Mo	Zr-0.5Cu, Zr-0.5Cu-0.5Mo Zr-1.0Cu, Zr-1.0Cu-0.5Mo	Tet. Zr_2Cu and cubic $ZrMo_2$ when Mo present	> 100	~0.5-2%
Zr-Sn-Nb	Zr-0.4Sn-0.2Nb, 0.4Sn-0.4Nb	no precipitates	N/A	N/A
Zr-Sn	Zr-0.2, 0.4, 0.8, 1.2 Nb	no precipitates	N/A	N/A
Reference Alloys	Sponge Zr, Crystal bar Zr, Zircaloy-4	no precipitates for Zr hcp C14 $Zr(Cr,Fe)_2$ for Zircaloy-4	80	~0.5 for Zircaloy-4
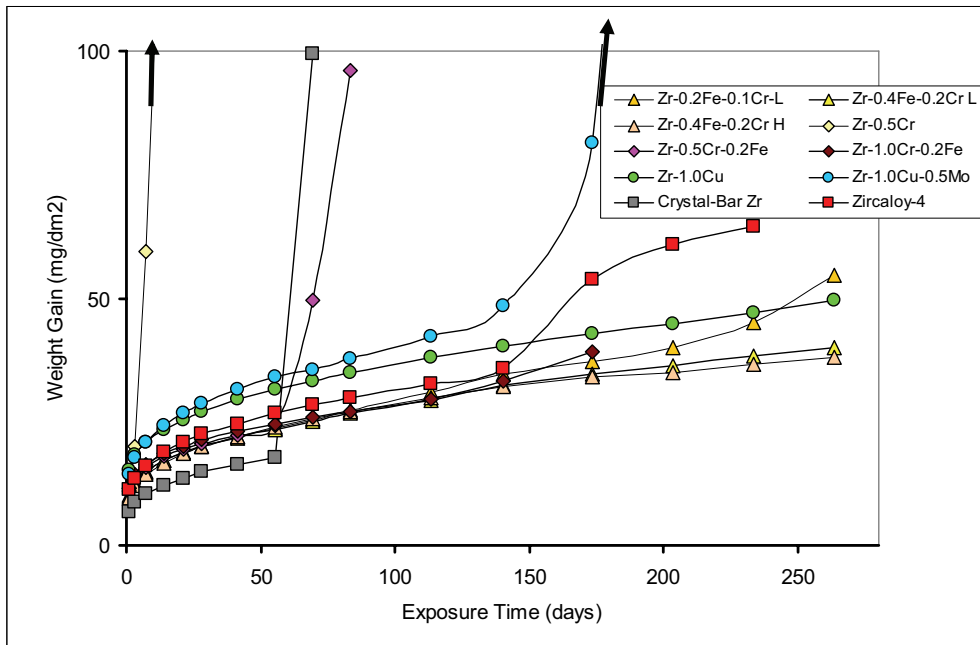
Figure 2: Weight gain vs. exposure time plot for the model alloys tested in 360 °C water.
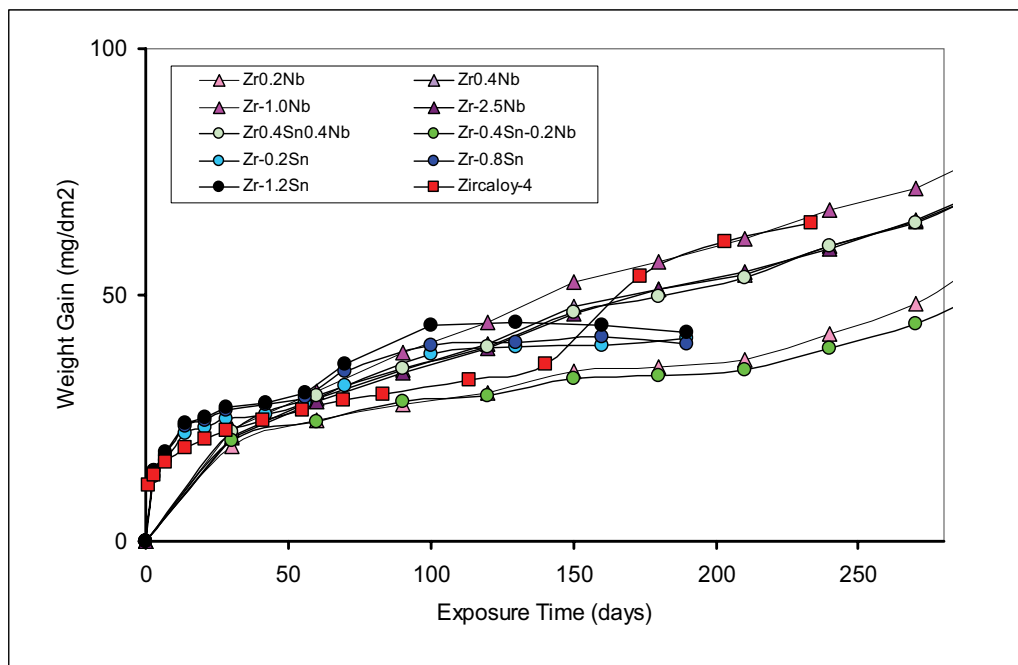
Figure 3: Corrosion weight gain for Zr-Nb, Zr-Nb-Sn and Zr-Sn model alloys tested in 360 °C pure water.

Results and discussion

The results of corrosion tests showed that the oxides remained adherent for most the samples and the corrosion weight gain provided a good measure of the oxide thickness. The rate-limiting step in the corrosion process likely involves transport of corrosion species through the oxide, because as the oxide layer grows the corrosion rate decreases, as discussed below.

The corrosion weight gains for the model alloys tested in pure water are plotted versus exposure time in Figure 2 (alloys with Cr, Fe, Cu and Mo, as well as pure Zr) and Figure 3 (alloys with Nb and Sn). For comparison, the weight gain observed on a batch with a composition of Zircaloy-4, manufactured in the same way as the alloys in this work, is also shown in the plots. The alloys in figure 1 show clearly differentiated behavior. The Zr-Fe-Cr alloys exhibit the slowest corrosion rate, with Zr-Cu showing the next lowest and several alloys exhibiting breakaway corrosion behavior. The Zircaloy-4 sample exhibits the classical behavior of forming a protective oxide that slows down the initially fast corrosion behavior creating nearly sub-cubic kinetics. After approximately 150 days there is an increase in the corrosion rate, associated with the loss of protectiveness at the oxide transition. This is followed by the reconstruction of the protective oxide, and the re-establishment of the same kinetics exhibited before the transition. The oxide growth is stable and the appearance of the oxide is black and shiny (although it becomes a little lighter in color after the transition).

In contrast, pure Zr showed non protective (breakaway) behavior right from the beginning of the corrosion test or after short exposures of about 50 days. No significant difference was seen between crystal bar and sponge Zr, indicating that the higher impurity level of sponge Zr (~ 600 wt. ppm Fe

versus 100 wt. ppm Fe) did not affect corrosion behavior. At breakaway, the oxide growth was characterized by a rapid acceleration of the weight gain without formation of a protective oxide. When breakaway occurs, the oxide becomes white (characteristic of a porous, non-protective oxide and which allows stoichiometric ZrO_2 - white in color - to be formed) and oxide spalling can occur [22]. We term this phenomenon "breakaway corrosion", as distinguished from an oxide transition which recovers stable growth.

Some alloys, especially among the "precipitate forming" alloys, exhibited breakaway corrosion. For the Zr-Cr-Fe model alloys, Zr-0.5Cr showed unstable oxide growth from the beginning of the test, while Zr-0.5Cr-0.2Fe showed breakaway, but at a later stage (after 50 days, similar to Zr), and Zr-1.0Cr-0.2Fe showed stable oxide growth. The alloys in the Zr-Cu-Mo system showed poor corrosion behavior in the presence of Mo, but the Zr-1.0 Cu alloy showed protective oxide growth. The best performing alloys in this test were the Zr-Fe-Cr alloys which all showed a stable oxide and protective behavior for the full period tested. In the better-performing alloys neither the oxide transition nor corrosion breakaway were seen for the period tested. No significant difference was observed between the four Zr-Fe-Cr alloys despite different precipitate sizes (such as the alloys treated at 720 °C and 580 °C, Table 1) and precipitate volume fraction (for example Zr-0.4Fe-0.2Cr vs. Zr-0.2Fe-0.1Cr).

In contrast with the precipitate forming alloys, the alloys with significant solute in the Zr matrix (Nb and Sn alloys) did not exhibit breakaway corrosion for any of the samples during the exposure time. For the Zr-Sn alloys, higher initial corrosion rates were seen, and an oxide transition was observed around 60 days exposure. It is also clear that some weight loss occurs after 120 days, likely due to oxide spalling. In the Zr-Nb system, the Zr-0.2Nb alloy showed lowest corrosion behavior,

and not much dependence of corrosion rate with Nb content between 0.4 and 2.5 Nb. No clear oxide transition was observed in the Nb alloys. The ZrNbSn alloys showed an oxide transition but exhibited corrosion rates that were similar to the equivalent Zr-Nb alloys of the same Nb content.

To characterize the corrosion kinetics in more detail, the measurements of the corrosion weight gain during pre-transition (up to 40 days exposure) were fit using a law of the type

$$W = At^n \qquad (1)$$

where W is the weight gain (mg/dm^2), t is the exposure time (days) and A and n are constants. For the alloys in this study, the power law in Equation 1 provided an excellent fit to the corrosion results (R^2 values were consistently near 0.99). Similar values of A and n were obtained using weight gains of the individual samples or the average weight gain of approximately eight samples. This shows that the results are consistent from sample to sample with low variability in the corrosion results, especially in the pre-transition regime.

The values of A and n calculated using this procedure are shown in Table 2. The values of n are almost all below 0.5, with some significantly lower (~0.18), indicating a significant deviation from a pure diffusion based process and consequent

parabolic behavior. The reason for these departures is not clear, but could be related to factors that hamper diffusion. These could include the presence of lateral cracks which serve as obstacles to oxygen ion migration, increasing grain size within the oxide could reduce grain boundary diffusion [7, 8], or the presence of stress, all of which can slow down diffusion and affect the value of n. Another possibility is related to the fact that the protective layer of the oxide is only a fraction of the measured oxide layer [9]; if this fraction changes (increases) with thickness then kinetics lower than parabolic could be established. Finally, it is possible that slower electron transport through the oxide layer slows down oxygen ion transport [10].

It is noteworthy that the values of n shown in Table 2 are characteristic of each alloy. The Zr-Nb samples have an average n of 0.42, reasonably close to parabolic. In the Zr-Sn alloys the average n is 0.32 and for ZrNbSn it is 0.41. In contrast, for the precipitate forming alloys, including Zircaloy the value of n is closer to 0.2.

In comparing Zircaloy-4 with the model alloys made from its individual constituents (Sn, Fe, Cr), it is possible to observe that an alloy with the same Fe-Cr content as Zircaloy behaves quite well, and does not show an oxide transition within the time tested. At the same time the Zr-Sn alloys show a transition, but not breakaway.

Table 2: Calculated Values of A and n for each alloy

Alloy Group	Alloy	A	n	ave. A	ave. n
Zr-Fe-Cr	Zr-0.2Fe-0.1Cr, 580	10.2	0.20	9.89	0.21
	Zr-0.2Fe-0.1Cr, 720	10.2	0.20		
	Zr-0.4Fe-0.2Cr, 580	9.78	0.21		
	Zr-0.4Fe-0.2Cr, 720	9.39	0.22		
Zr-Cr-Fe	Zr-0.5Cr	non-protective		10.9	0.19
	Zr-0.5Cr-0.2Fe	11.5	0.17		
	Zr-1.0Cr	9.73	0.21		
	Zr-1.0Cr-0.2Fe	11.6	0.18		
Zr-Cu-Mo	Zr-0.5Cu	13.6	0.17	14.1	0.18
	Zr-0.5Cu-0.5Mo	13.6	0.17		
	Zr-1.0Cu	15.1	0.17		
	Zr-1.0Cu-0.5Mo	14.0	0.21		
Zr	Sponge Zr	8.50	0.20	7.56	0.22
	Crystal Bar Zr	6.61	0.24		
Zircaloy	Zircaloy-4	11.0	0.21	10.20	0.22
	Zr-4 Control	9.40	0.23		
Zr-Sn	Zr-0.2Sn	9.30	0.29	9.50	0.29
	Zr-0.4Sn	8.10	0.32		
	Zr-0.8Sn	10.0	0.27		
	Zr-1.2Sn	10.6	0.27		
Zr-Sn-Nb	Zr-0.4Sn-0.2Nb	5.92	0.43	6.52	0.41
	Zr-0.4Sn-0.4Nb	7.11	0.39		
Zr-Nb	Zr-0.2Nb	6.40	0.43	5.92	0.45
	Zr-0.4Nb	5.00	0.52		
	Zr-1.0Nb	5.90	0.45		
	Zr-1.5Nb	5.80	0.44		
	Zr-2.5Nb	6.50	0.40		

Characterization of oxide layer texture with synchrotron radiation diffraction

Figure 3 shows a plot of x-ray intensity versus two theta angle obtained in reflection geometry, as a function of distance along the cross section of (a) an oxide formed on Zr-2.5Nb, which exhibits good corrosion behavior and (b) an oxide formed on Zr-0.5Cr in steam which shows poor corrosion behavior. The peaks are indexed as shown in the figure. The location of the peaks determined manually by deconvoluting the pattern using PeakFit4.0, with a Pearson VII peak shape, corresponded quite well with the known peak locations as mentioned previously [4]. The point labeled "0" is the oxide metal interface, similarly to [3]. The location of the oxide layer interfaces with the metal and water was determined with good precision using x-ray fluorescence [3]. These interfaces correspond well with the locations in the oxide where the diffraction pattern changes from peaks characteristic of the hcp Zr metal to the peaks characteristic of the monoclinic and tetragonal zirconium oxide phases. All the observed peaks were indexed as one of these phases. In the following a subscript "M" indicates the monoclinic zirconia phase and "T" the tetragonal zirconia phase.

As can be noticed in Figure 4(a), the phases present and their orientation change with distance from the oxide-metal interface. In particular, the intensity of the $(020)_M$ peak varies with distance in a periodic manner. This is in agreement with the previously observed periodic variation of the oxide orientation across the thickness of the oxide layer. The growth direction of the oxide has been identified in previous work [11, 12] as being close to the $(200)_M$ pole of the monoclinic phase. The direction of the $(020)_M$ and $(002)_M$ monoclinic poles are therefore close to being in the plane of the oxide-metal interface and aligned preferentially with the tangential and rolling directions. The period of the variations of the $(020)_M$ intensity has been shown to correspond closely with the thickness of the oxide transition. More specifically, at locations close to the oxide transition the alignment of the $(020)_M$ and $(002)_M$ poles with the tangential and rolling directions is lost as the diffracted intensities of these two peaks are more randomly distributed in the transverse x rolling plane. The locations in the oxide layer where the $(020)_M$ and $(002)_M$ peaks are higher correspond to places where the tetragonal peaks are low (in the case shown in Figure 4 the tetragonal phase fraction is small overall) . This has been interpreted as meaning that, at the transition, the tetragonal phase is formed more easily, as greater access of water (or oxygen) to the underlying metal creates a higher nucleation rate of new grains which because of their small size tend to be tetragonal rather then monoclinic. Another interesting aspect of Figure 4 (a) is the structure of the oxide near the oxide metal interface. The peak identified in the figure as $(002)_T$ is an indicator of a highly oriented tetragonal phase that exists near the oxide-metal interface [3]. This phase is thought to be a precursor of the monoclinic phase, that is, the grain transforms to the monoclinic phase after a critical size and it is at the correct orientation to form the properly oriented monoclinic phase observed in the oxides.

The orientation relationship $(002)_T//(020)_M$ (known from reference [13]) is thus present across the interface and as a

result, a well-oriented oxide forms that leads to better corrosion behavior. A previous study has associated good corrosion behavior with well-aligned, long columnar grains [14]. Figure 5 shows a transmission electron micrograph taken from a Zr-0.4Nb after 150 days exposure in 360 °C water. An oxide about 2.2 microns has formed, and which consists mainly of long and wide columnar grains, which are well aligned, and show a small degree of grain-to-grain mis-orientation. This particular oxide was formed on Zr-2.5Nb, which shows normally lower values of the tetragonal fraction than oxides formed on Zircaloy-4 [15]. Accordingly the location of the 100% intensity diffraction peak $(101)_T$ shows very little intensity in Figure 3.
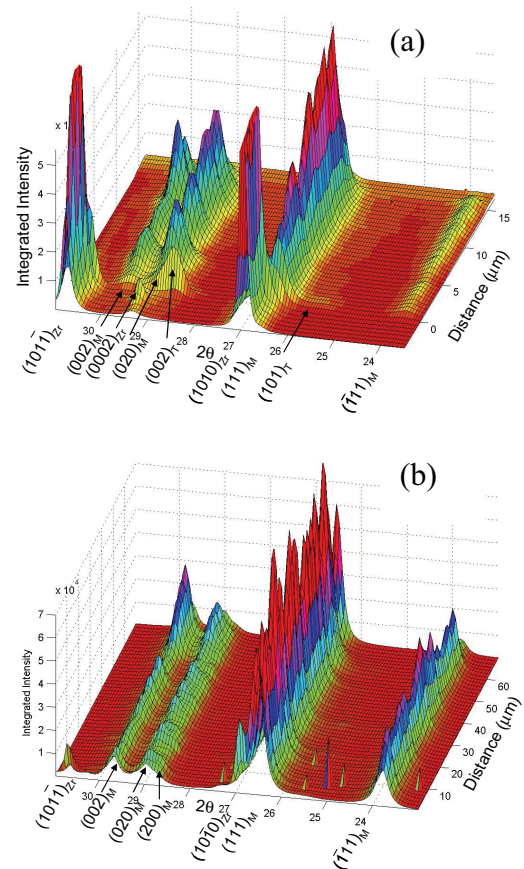

Figure 4: Intensity versus two theta angle versus distance showing phases present from oxide/metal interface to oxide/water interface of (a) Zr-2.5Nb oxide layer formed in 360 °C pure water; (b) Zr-0.5Cr in 500 °C steam environment.

In Figure 4 (b), the same phases are present, but a few important differences are seen. Firstly, although the $(020)_M$ and $(002)_M$ are also strong here, the ratio of I_{020M}/I_{002M} is markedly lower (it is approximately 1) and the $(002)_T$ structure is not present at the oxide-metal interface. Periodicity is also much less evident. All of these differences point to a less orderly oxide formation process, that is a process in which the oxide formed does not have the ideal structure, which leads to a less protective oxide layer.

Normally the characterization of oxide texture can only be achieved as an average over the whole oxide layer. To understand the oxide growth mechanism it is necessary to study the variation of these oxide orientations with distance from the oxide-metal interface. Using the transmission geometry shown in Figure 1 (b), it is possible to obtain pole figures for the various peaks of the different phases present in the oxide. Although this has not yet been done for the model alloys in this study, an example is shown of one such measurement performed on a commercial alloy ZIRLO. Figure 6 shows five of these pole figures generated on four planes of the monoclinic phase (200, 111 , $\bar{1}$11, and 002) and one for the tetragonal phase (101) for a specific point in the oxide layer formed on a ZIRLO sample [3].
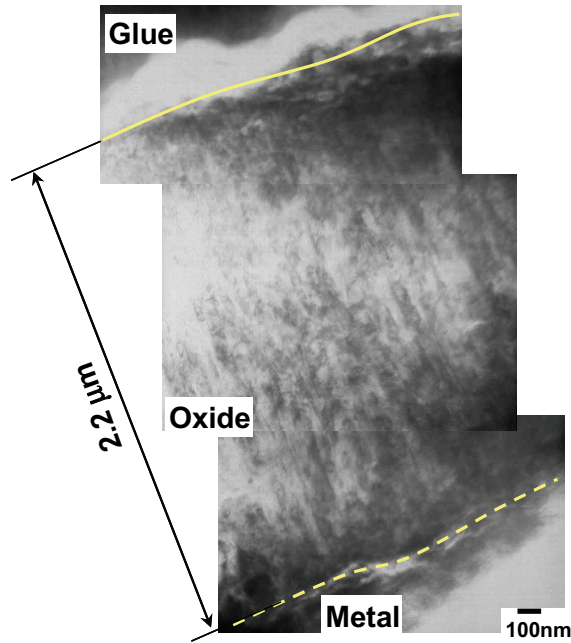

Figure 5: Composite transmission electron bright field micrograph of oxide layer formed in Zr-0.4Nb alloy after 150 days exposure in 360 °C pure water.

The normal direction (direction of oxide growth) is coming out of the paper, while the transverse direction of the tube and the axial direction are indicated on the figures. As previously reported, the $(200)_M$ peak is aligned close to the growth direction of the oxide (approximately 10 degrees) [12]. In agreement with previous studies, the 111 peaks are located in four lobes, about 55-60 degrees from the normal direction, in between the axial and transverse directions and the 111 poles are located in the same directions, but 40 degrees from the normal [21]. The $(200)_M$ and $(002)_M$ poles (the $(020)_M$ is not shown because it is difficult to deconvolute from the $(200)_M$ pole) are aligned in the transverse-axial plane, near the transverse (T) and axial (A) directions. Finally the tetragonal peak $(101)_T$ is aligned in between the $(111)_M$ and $(\bar{1}11)_M$ peaks as seen previously [14]. It has been shown previously that the following orientation relationships hold [13]:

$$(002)_T \, // (020)_M \qquad (2)$$

and it is also known [16]

$$(10\bar{1}0)\alpha\text{-Zr} \, // \, (020)_M \qquad (3)$$

and [17]

$$(0001)\alpha\text{-Zr} \, // \, (200)_M \qquad (4)$$

For the normal fabrication texture seen in Zircaloy tube or sheet, the $(10\bar{1}0)_{\alpha\text{-Zr}}$ poles are aligned with the axial or rolling direction, and thus the $(020)_M$ poles tend to be aligned along this same direction, and the $(002)_M$ aligned with the transverse direction. The as-fabricated metal texture has a large proportion of the basal planes aligned with the normal direction. In that orientation, the $(10\bar{1}0)_{\alpha\text{-Zr}}$ poles can be oriented close to the $(020)_M$ poles leading to a well-oriented oxide. Thus the common fabrication texture should be farmable for corrosion. This result is on agreement with previous observations that show a higher oxidation rate in the prism $11\bar{2}0$ direction than in the 0002 (basal) direction [18]. The observations shown here and in previous works indicate that there is a thin region in the first 0.2-0.3 microns near the oxide-metal interface where a highly oriented tetragonal phase is formed, and that serves as a precursor for the monoclinic phase [3]. This phase is observed in the examination of cross-sectional samples, the surface of which are aligned with the axial direction in tube samples but not in sheet samples in which the rolling direction is aligned with the normal to the sample surface (Figure 1 (a)).
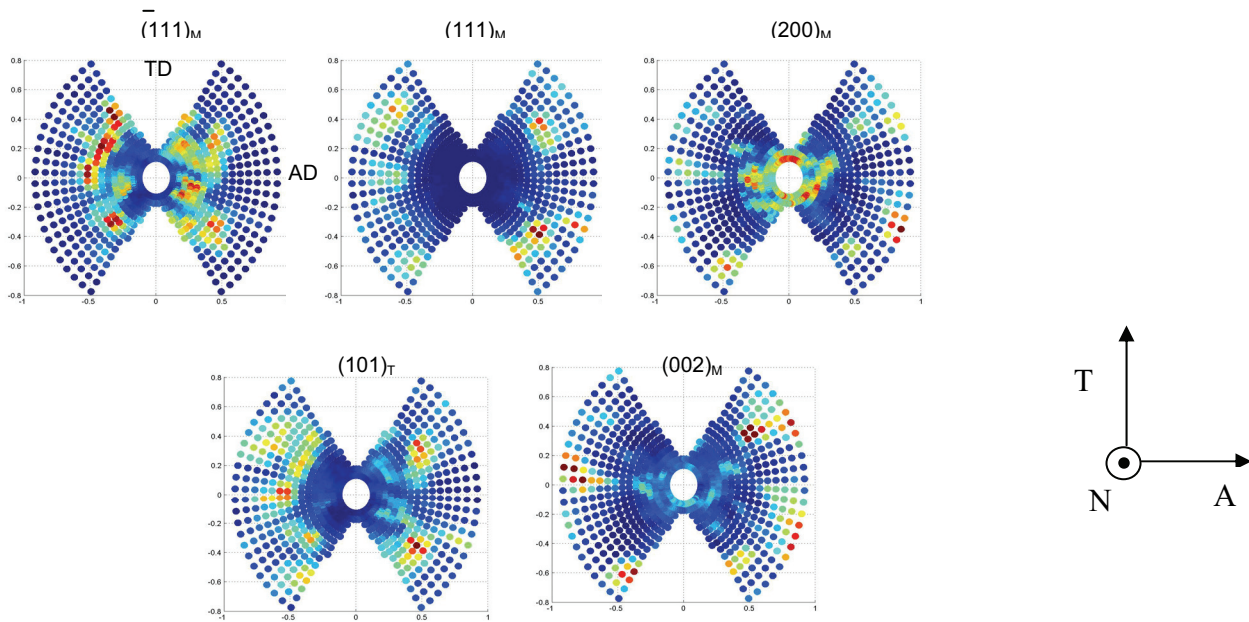
Figure 6: Pole figures for the $(1\ \bar{1}1)_M$, $(111)_M$, $(002)_M$ and $(200)_M$ monoclinic and $(101)_T$ tetragonal oxide planes in a 16.4 micron thick ZIRLO oxide layer taken at a position located 1.8 micron from the oxide metal interface (T indicates transverse direction, N is normal and A is axial directions).

The $(002)_T$ peak visible in Figure 4a appears in tube samples but not in sheet samples (fig. 4b) , in agreement with the $10\bar{1}0$ hcp pole being aligned with the axial direction in tube samples but 30 degrees form the rolling direction in sheet samples. It should also be noted that the ratio of the intensity of $(020)_M$ and $(002)_M$ is about 3 when the highly oriented tetragonal phase is present and about 1 when it is absent, again pointing to the orientation relationship shown in equation 3. The presence of a well-aligned texture in the oxide has been linked with good corrosion behavior [3].

Another difference which is not immediately apparent in Figure 4 (b), is that compared to well-behaved oxides, in the Zr-0.5Cr sample, the $(200)_M$ pole shows significant intensity in the measurement configuration shown in Figure 1 (a) which means that many $(200)_M$ poles are aligned in the direction perpendicular to the oxide cross section (other information allows us to identify that orientation as close to the direction of oxide growth [6]). Figure 7 shows the diffracted intensity versus two-theta angle taken from oxides formed on two model alloys at a location 1.2 microns from the oxide metal interface. The angular range corresponding to the monoclinic oxide {200} family of peaks [(200)_M, (020)_M and (002)_M] is shown in the figure. The diffraction geometry used is that shown in Figure 1 (a), and as a result the growth direction of the oxide is perpendicular to the diffraction vector. If the oxide is oriented with the $(200)_M$ pole close to the oxide growth direction, then the $(200)_M$ should be absent from this pattern. The oxides that show good corrosion behavior normally show such an orientation. The oxide formed in Zr-0.5Cr in water shown in Figure 7(a) has significant $(200)_M$ intensity, indicating that oxide is not so highly textured, i.e. some of the $(200)_M$ planes have their poles in the cross-

sectional plane of the oxide. This alloy oxide sample was taken from a corrosion sample that showed significant corrosion weight gain. In contrast the pattern shown in Figure 7 (b), taken from a Zr-0.5Cr-0.2Fe sample shows no $(200)_M$ peak intensity indicating that none of the $(200)_M$ poles are aligned in the cross sectional direction. These results suggest that the presence of Fe altered the texture of the resulting oxide, creating an oxide with a structure that is more conducive to stable oxide growth (although in this case, the onset of breakaway is merely delayed).

Tetragonal Phase Fraction

Although the tetragonal phase has often been associated with a protective oxide, it is not clear whether the oxide protectiveness is a cause or an effect of tetragonal oxide. It has however, been shown that among Zircaloy-4, ZIRLO and Zr-2.5Nb the higher the tetragonal fraction the higher the corrosion rate [4].

In any case, the presence of the tetragonal phase, and specially, its distribution within the oxide layer, can give clues as to the mechanism of advancement of the oxide. In particular it has been proposed that a highly oriented tetragonal phase exists at the oxide-metal interface and which serves as a precursor for the well-oriented monoclinic oxide that subsequently forms [3]. The tetragonal phase can be stabilized by small grain size [19], stresses [20], sub-stoichiometry and the presence of alloying elements. Since many of these appear in protective oxides, the association between protective oxides and high tetragonal fraction is natural.
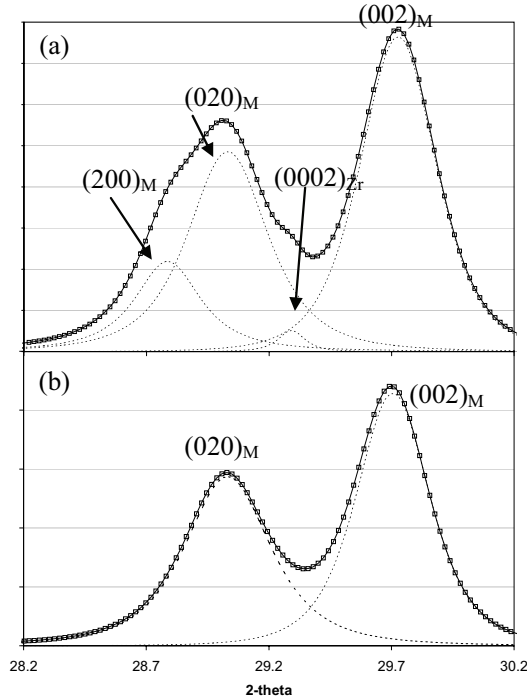
Figure 7: Intensity versus two-theta angle for the $(200)_M$ family of planes 1.2 micron away from the oxide-metal interface. (a) Zr-0.5Cr oxide formed in 360 ^{o}C water showing a shoulder corresponding to the $(200)_M$ peak. (b) Zr-0.5Cr-0.2Fe oxide formed in 360 ^{o}C water does not show the $(200)_M$ peak.

It is a common observation that the tetragonal phase fraction is higher near the oxide-metal interface. This has been explained as a result of smaller grains being formed with the new oxide at the oxide-metal interface [3]. The calculation of the tetragonal fraction is performed using the Garvie-Nicholson formula:

$$f_T = \frac{I_{101}^{T}}{I_{111}^{M} + I_{101}^{T} + I_{\bar{1}11}^{M}} \tag{5}$$

However, because this formula is strictly valid only for powder samples, a texture correction has to be performed for the textured oxides studied here as described in [4]. Alternatively, by acquiring the intensities over the pole figures shown in Figure 6, the texture correction is not necessary. Figure 8 shows the tetragonal fraction calculated with such a procedure, i.e. integrating the intensities of the three peaks in equation 2 over all orientations. Good agreement is found with the values previously calculated using a texture correction.

Overall no significant difference has yet been seen among the tetragonal fractions seen in the oxides formed on the different model alloys. Calculations performed from measurements using the 1 micron beam, indicate that the tetragonal fraction averaged over the oxide layer is approximately 6-7%, both for Zr-Nb alloys and for Zr-1.0Cr-0.2Fe alloy.
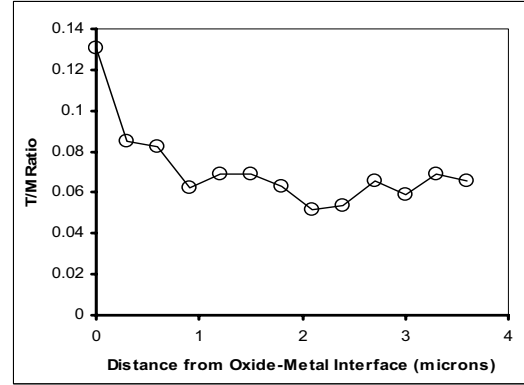

Figure 8: Tetragonal fraction calculated using the pole figures in Fig.6, obtained with microbeam transmission geometry.

Conclusions

A comprehensive study of the effects of alloying elements and metal microstructure on the corrosion process in Zr alloys is being undertaken. Several alloys forming both solid solutions and precipitates in the Zr matrix have been autoclave corroded in 360 ^{o}C pure water static autoclaves for periods up to 250 days. Oxide samples have been systematically archived for detailed study using advanced characterization techniques. The aim is to elucidate the connection of the oxide structure with the corrosion rate observed in the alloys. The main conclusions are as follows:

1. Significant differences are observed in the corrosion behavior of the various alloys. These differences manifest themselves both in the tendency to exhibit breakaway behavior and in the clear separation of the value of the exponent n among the various alloys.

2. The examination of these oxides using synchrotron radiation diffraction shows a complex structure with a mixture of tetragonal and monoclinic oxide. The monoclinic oxide show a well-established preferential orientation with the growth direction aligned approximately 10 degrees from the $(200)_M$ direction and the $(020)_M$ direction approximately parallel to $10\bar{1}0_{hcp}$. This preferential orientation of the monoclinic oxide is less apparent in alloys following breakaway corrosion.

3. A structure exists near the oxide metal interface that includes a $(002)_T$ peak which serves as a precursor for the formation of the highly textured monoclinic phase with the $(020)_M$ pole parallel to the $(002)_T$.

4. The methods developed here showed the possibility for the first time of obtaining pole figures for the oxide as a function of distance from the oxide metal interface, for layers as small as 0.2 microns wide, and thus to understand the oxide structure formation at a fundamental level.

5. The structure of the model alloy oxides is similar to the

structure of commercial alloys studied before. More detailed examination of the model alloys will be performed by other techniques to confirm.

Acknowledgments

References

[1] D. Franklin, "Zirconium Alloy Corrosion: A Review based on an International Atomic Energy Agency Meeting," 9th International Symposium on Zr in the Nuclear Industry, 1993, ASTM STP 1132, 3.

[2] S. Kass, "The Development of the Zircaloys," Symposium on Corrosion of Zirconium Alloys, ANS Winter meeting, 1963, New York, 1964, ASTM, STP 368, 3-27.

[3] A. T. Motta, A. Yilmazbayhan, R. J. Comstock, J. Partezana, S. G.P., Z. Cai., and B. Lai, "Microstructure and Growth Mechanism of Oxide Layers Formed in Zr Alloys Studied with Micro Beam Synchrotron Radiation," *Journal of ASTM International*, vol. 2, Paper # JAI 12375, 2005.

[4] A. Yilmazbayhan, A. T. Motta, R. J. Comstock, G. P. Sabol, B. Lai, and Z. Cai, "Structure of Zirconium Alloy Oxides formed in pure water studied with Synchrotron radiation and optical microscopy: relation to corrosion rate," *Journal of Nuclear Materials*, vol. 324, pp. 6-22, 2004.

[5] K. T. Erwin, O. Delaire, A. T. Motta, R. C. Birtcher, Y. Chu, and D. Mancini, "Observation of second-phase particles in bulk zirconium alloys using synchrotron radiation," *Journal of Nuclear Materials*, vol. 294, pp. 299-304, 2001.

[6] A. T. Motta, K. T. Erwin, O. Delaire, R. C. Birtcher, Y. Chu, J. Maser, D. C. Mancini, and B. Lai, "Synchrotron Radiation Study of Second Phase Particles and Alloying Elements in Zirconium Alloys," Zirconium in the Nuclear Industry: 13th International Symposium, Annecy, France, 2001, ASTM, STP 1423, 59-78.

[7] G. P. Sabol and S. G. McDonald, "Structural Aspects of Oxide Film Growth on Zirconium-Based Alloys," Stress Effects and the Oxidation of Metals, New York, NY, 1975, American Institute of Mining, Metallurgical and Petroleum Engineers, 353.

[8] G. P. Sabol and S. B. Dalgaard, "The Origin of the Cubic Rate law in Zirconium Alloy Oxidation," *Journal of the Electrochemical Society*, vol. 122, pp. 316, 1975.

[9] P. Barberis and A. Frichet, "Characterization of Zircaloy-4 oxide layers by impedance spectroscopy," *Journal of Nuclear Materials*, vol. 273, pp. 182-191, 1999.

[10] B. Cox, "Some thoughts on the mechanisms of in-reactor corrosion of zirconium alloys," *Journal of Nuclear Materials*, vol. 336, pp. 331-368, 2005.

[11] H. Li, H. M. Glavicic, and J. A. Spuznar, "A Model of Texture formation in ZrO2 Films," *Materials Science and Engineering*, vol. A366, pp. 164-174, 2004.

[12] N. Petigny, P. Barberis, C. Lemaignan, C. Valot, and M. Lallemant, "In situ XRD analysis of the oxide layers formed by oxidation at 743 K on Zircaloy-4 and Zr-1NbO," *Journal of Nuclear Materials*, vol. 280, pp. 318-330, 2000.

[13] E. C. Subbarao, H. S. Maiti, and K. K. Srivastava, "Martensitic Transformation in Zirconia," *Physica Status Solidii*, vol. 21, pp. 9-39, 1974.

[14] A. Yilmazbayhan, E. Breval, A. Motta, and R. Comstock, "Transmission Electron Microscopy Examination of Oxide Layers Formed in Zr Alloys," *Submittedl to the Journal of Nuclear Materials*, 2005.

[15] P. Bossis, J. Thomazet, and F. Lefebvre, "Study of Mechanisms Controlling the Oxide Growth Under Irradiation: Characterization of Irradiated Zircaloy-4 and Zr-1Nb-O Oxide Scales," Zirconium in the Nuclear Industry: Thirteenth International Symposium, Annecy, France, 2001, ASTM, STP 1423, 190-221.

[16] J. E. Bailey, "On the oxidation of thin films of zirconium," *Journal of Nuclear Materials*, vol. 8, pp. 259, 1963.

[17] F. W. Vahldiek, "Epitaxial Oxidation of Zirconium at Various Temperatures," *Journal of Less-common Metals*, vol. 12, pp. 19, 1967.

[18] H. G. Kim, T. H. Kim, and Y. H. Jeong, "Oxidation Characteristics of basal (0002) plane and prism (1120) plane in HCP Zr," *Journal of Nuclear Materials*, vol. 306, pp. 44-53, 2002.

[19] R. C. Garvie, "Stabilization of the Tetragonal Structure in Zirconia Microcrystals," *The Journal of Physical Chemistry*, vol. 82, pp. 218-224, 1978.

[20] J. Godlewski, "How the Tetragonal Zirconia is Stabilized in the Oxide Scale that is Formed on a Zirconium Alloy Corroded at 400 C in steam," 10th Int. Symp. on Zr in the Nuclear Industry, 1994, ASTM, STP 1245, 663-686.

[21] J. L. Bechade, R. Dralet, P. Goudeau, and P. Yvon, "Studies of Zirconium alloy oxide layers using synchrotron radiation," *Materials Science Forum*, vol. 347-349, pp. 471-478, 2000.

[22] D. L. Douglass, *The Metallurgy of Zirconium*. Vienna: International Atomic Energy Agency Supplement, 1971.